

# Multi-type sensor placement and response reconstruction for building structures: Experimental investigations

Rong-Pan Hu<sup>†</sup>, You-Lin Xu<sup>‡</sup> and Sheng Zhan<sup>§</sup>

*Department of Civil and Environmental Engineering, The Hong Kong Polytechnic University, Hong Kong, China*

**Abstract:** Estimation of lateral displacement and acceleration responses is essential to assess safety and serviceability of high-rise buildings under dynamic loadings including earthquake excitations. However, the measurement information from the limited number of sensors installed in a building structure is often insufficient for the complete structural performance assessment. An integrated multi-type sensor placement and response reconstruction method has thus been proposed by the authors to tackle this problem. To validate the feasibility and effectiveness of the proposed method, an experimental investigation using a cantilever beam with multi-type sensors is performed and reported in this paper. The experimental setup is first introduced. The finite element modelling and model updating of the cantilever beam are then performed. The optimal sensor placement for the best response reconstruction is determined by the proposed method based on the updated FE model of the beam. After the sensors are installed on the physical cantilever beam, a number of experiments are carried out. The responses at key locations are reconstructed and compared with the measured ones. The reconstructed responses achieve a good match with the measured ones, manifesting the feasibility and effectiveness of the proposed method. Besides, the proposed method is also examined for the cases of different excitations and unknown excitation, and the results prove the proposed method to be robust and effective. The superiority of the optimized sensor placement scheme is finally demonstrated through comparison with two other different sensor placement schemes: the accelerometer-only scheme and non-optimal sensor placement scheme. The proposed method can be applied to high-rise buildings for seismic performance assessment.

**Keywords:** experimental investigation; multi-type sensors; inclinometer; response reconstruction; optimal sensor placement

## 1 Introduction

With the rapid growth of population in mega cities, a large number of high-rise buildings have been built around the world. These buildings are subjected to various loading conditions including earthquake excitation. The safety and serviceability of building structures has thus gained much attention. Long-term structural health monitoring (SHM) systems have also been developed to provide real-time measurements of various external loadings and structural responses, which are expected to be used for the performance evaluation of high-rise buildings. However, the number of sensors is always limited in consideration of the huge size and complex structural system of high-rise buildings. Accurate

and complete structural performance evaluation is almost impossible by just utilizing direct measurement information from installed sensors. This is particularly true for important but inaccessible structural locations. Recently, a feasible and cost-effective way of solving the problem has been proposed by integrating response reconstruction algorithm with optimal sensor placement scheme in such a way that the optimized sensor placement configuration enables the best estimation of structural responses at all interested locations.

Yi *et al.* (2011) proposed an optimal sensor placement method for high-rise buildings based on the generalized genetic algorithm, but they dealt with single type of sensor. An integrated optimal sensor placement and response reconstruction method has been proposed for long-span bridges equipped with multi-type sensors by Xu *et al.* (2016). Corresponding experiments have also been conducted on a two-pin-supported overhanging beam and a test-bed of long-span suspension bridge (Zhu *et al.*, 2013; Xu *et al.*, 2016). Zhang and Xu (2016) further developed this method for the structure under unknown excitation by incorporating the excitation estimation process. However, the method designed for long-span bridges may not be applicable for high-rise buildings, for the two different types of structures adopt quite different sensor systems and

**Correspondence to:** You-Lin Xu, Department of Civil and Environmental Engineering, The Hong Kong Polytechnic University, Hong Kong, China

Tel: (+852) 27666050; Fax: (+852) 22641671

E-mail: ceylxu@polyu.edu.hk

<sup>†</sup>PhD Candidate; <sup>‡</sup>PhD, Chair Professor; <sup>§</sup>Research Fellow

**Supported by:** The Hong Kong Polytechnic University through the group project “Fundamentals of Earthquake Engineering for Hong Kong” (4-ZZCD) and the collaborative research project with Beijing University of Technology (4-ZZGD)

**Received** November 15, 2017; **Accepted** December 15, 2017

the corresponding responses also differ from each other. Commonly-used accelerometers for dynamic responses measurements may not be appropriate for monitoring static and quasi-static deformation of high-rise buildings of long natural periods. Instead, GPS and inclinometers are more effective sensors for monitoring high-rise building deformation (Yigit *et al.*, 2010; Li *et al.*, 2010; Su *et al.*, 2013) because the safety of a high-rise building is normally evaluated in terms of its inter-story drift. In this connection, the authors have proposed an integrated multi-type sensor placement and response reconstruction method for building structures under unknown excitation on basis of the Kalman filter algorithm (Hu *et al.*, 2017). In this method, the multi-type response measurements from GPS receivers, accelerometers, and inclinometers are fused together to provide an optimal state and excitation estimate leading to the minimum estimation error covariance. The minimum number and optimal placement of multi-type sensors are determined by an iterative process where the estimation error decreases with the increase of candidate sensor number. Unmeasured responses at critical locations without sensors and ground motion excitation can then be reconstructed based on the optimal structural state and excitation estimate. Nevertheless, experimental validation should be conducted before this method can be applied to real building structures.

This paper thus presents an experimental investigation to validate the proposed multi-type sensor optimal placements and response reconstruction method. A steel cantilever beam was manufactured and installed in the laboratory. A sensory system, a data acquisition and processing system, and an excitation actuator were arranged accordingly. Since the inclinometer could not be directly mounted on the steel cantilever beam due to its disproportionate size and mass, an alternate technique for measuring the rotational angle was adopted. A finite element (FE) model of the cantilever beam was established and updated using the modal test data. After the optimal sensor placement for multi-type sensors were determined based on the updated FE model and using the proposed method, the corresponding sensors were installed on the physical beam. Additional sensors were also installed on the beam to record the responses for the comparison of reconstructed and measured responses in order to verify the effectiveness and feasibility of the proposed method.

Additional experimental investigations were also conducted to check the robustness and applicability of the proposed method in various situations. Random excitations with three different bandwidths were applied separately to excite the physical beam to investigate the effect of excitation frequency on the response estimation. Response reconstruction under unknown excitation was performed to manifest the potential of the method for estimating both response and excitation simultaneously. Two additional sensor placement strategies, namely

the accelerometers-only placement and non-optimal sensor placement strategies, were also investigated and the results were compared with the optimal sensor placement scheme to demonstrate the impact of sensor types and sensor locations on the accuracy of response reconstruction.

## 2 Experimental Setup

In this section, the experimental setup, including a cantilever beam, excitation system, sensor system, and measurement system, is introduced.

### 2.1 Cantilever beam

In consideration that most of high-rise buildings are flexible with a long fundamental period, a slender steel cantilever beam was selected and used in this experimental investigation (see Fig. 1). The height of the steel beam is 1.6 m and the cross-sectional area of the beam is  $b$  (width)  $\times h$  (thickness) =  $50 \times 6 \text{ mm}^2$ . The one end of the beam was fixed to the laboratory ground via a thick steel plate. The elastic modulus of the steel is 2.06 GPa and the density is  $78000 \text{ kg/m}^3$ . An upright stanchion was set up in line with the cantilever beam for installing the laser meters.

### 2.2 Excitation system

The excitation system consisted of a LDS (V406 M4-CE) exciter (see Fig. 2(a)), a B&K signal generator (see Fig. 2(c)) and a LDS PA500 power amplifier (see Fig. 2(d)). Random excitations with different amplitudes and frequency ranges could be generated and applied to the cantilever beam. To make less influence on the dynamic properties of the cantilever beam, the exciter was connected to the beam at a height of 100 mm above the ground via a soft spring. A B&K 8200 force transducer weighing 21 g (see Fig. 2(b)) was installed between the beam and the spring to directly measure the input force on the beam.

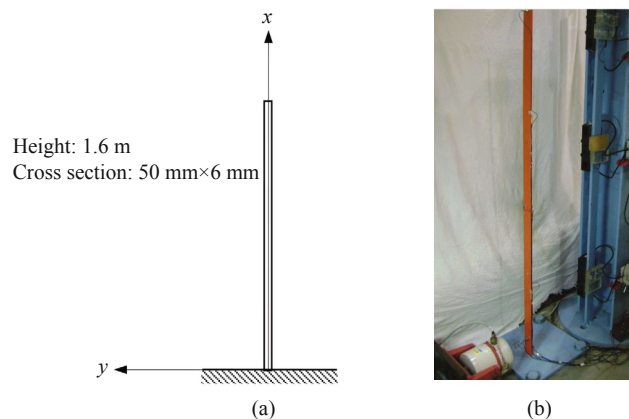


Fig. 1 Setup of the cantilever beam: (a) sketch view (b) lab view

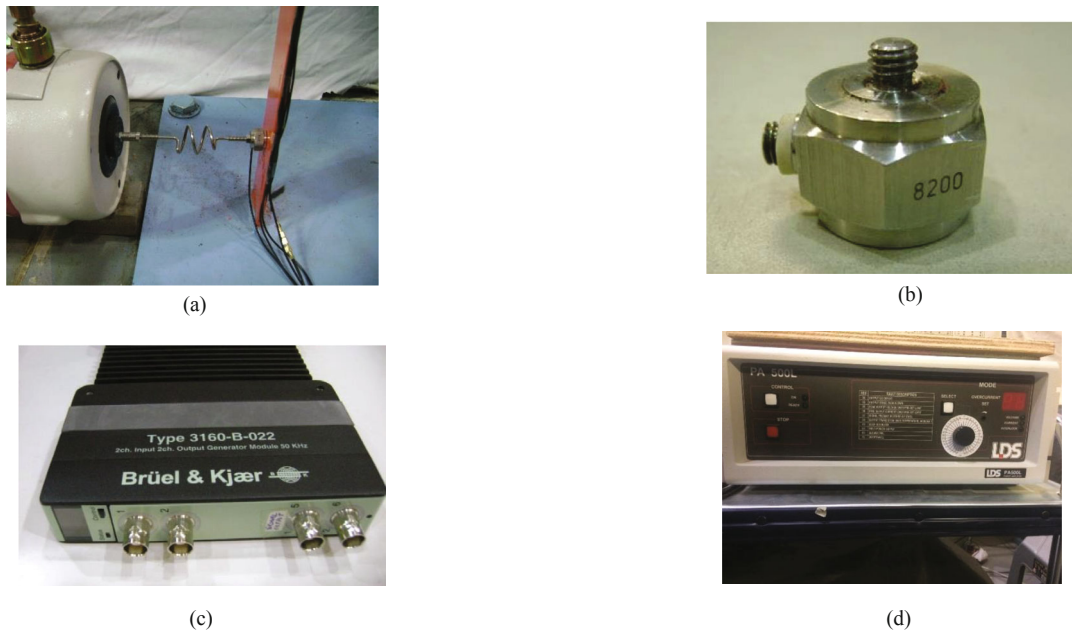


Fig. 2 Excitation system: (a) electromagnetic vibrator; (b) force transducer; (c) signal generator; (d) power amplifier

### 2.3 Sensor system

A total of six KD1000B accelerometers (see Fig. 3(a)) were utilized to measure the acceleration responses of the beam at six locations. The mass of each accelerometer is 1.2 g and its influence on the dynamic properties of the cantilever beam is very small. Six LK-503 laser displacement meters (see Fig. 3(b)) were used to directly measure the horizontal displacement responses and to indirectly measure the rotational angles of the cantilever beam at three locations.

It is difficult to directly measure the rotational angles of the beam because the weights of inclinometers could distort the original dynamic properties of the beam severely if they are mounted on the beam. Thus, an alternate measurement technique is used, in which the displacements of two adjacent points of the beam were measured by the two laser meters (see Fig. 3(b) and Fig. 5(b)) and then the secant of the two points was calculated as a substitution of the rotational angle. The calculation of the rotational angle is shown in Fig. 4.

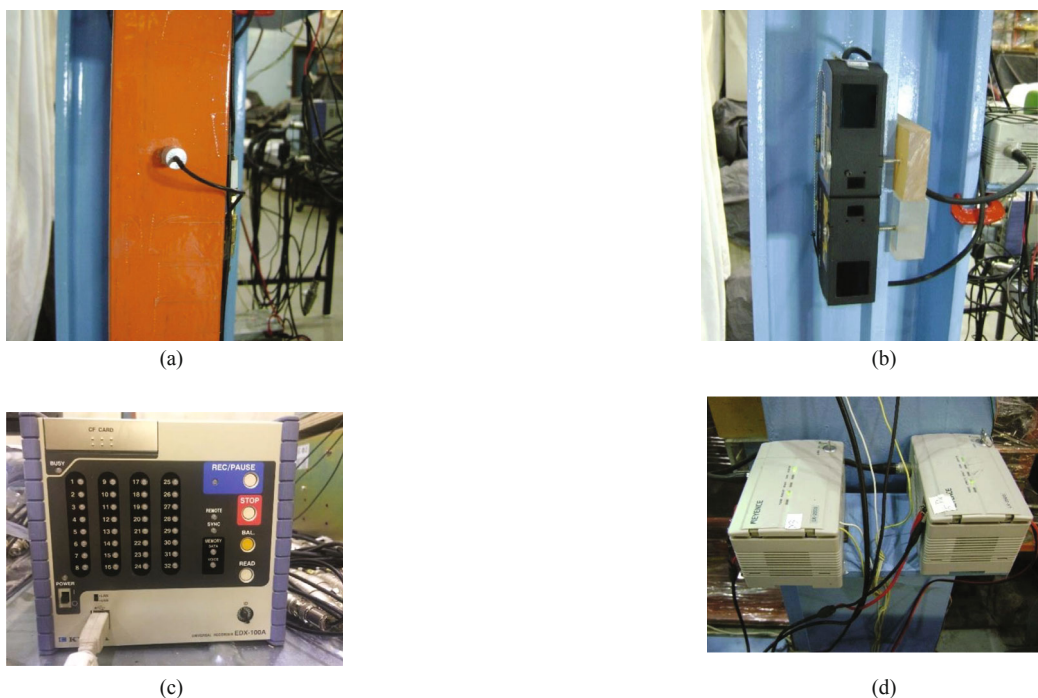


Fig. 3 Sensor system: (a) accelerometer; (b) laser meter; (c) data recorder; (d) signal conditioner for laser meter

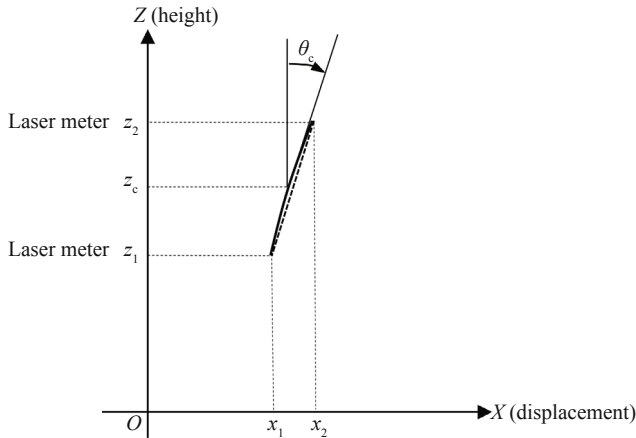


Fig. 4 Sketch of measurement for inclination angle

In practice and also in the laboratory experiment, the rotational angle  $\theta_c$  at the middle point  $z_c$  of the beam between the measurement points  $z_1$  and  $z_2$  is very small, and it could be approximated by the corresponding tangent slope.

$$\theta_c \approx \tan(\theta_c) \quad (1)$$

Since the distance between the two adjacent points are short compared with the total height of the beam and the rotational angle is very small, the deformation of the beam between  $z_1$  and  $z_2$  could be assumed as linear. Thus, the tangent slope could be substituted by the secant slope:

$$\tan(\theta_c) \approx \frac{\Delta x}{\Delta z} = \frac{x_2 - x_1}{z_2 - z_1} \quad (2)$$

The two-adjacent laser displacement meters used to measure the rotational angle are referred as “one inclinometer” in the following section. Thus, three inclinometers are used in this experimental investigation. Besides, the two-adjacent laser displacement meters could also provide the horizontal displacements of the two points on the beam, which can be used in the response reconstruction or to check the accuracy of the response reconstruction.

## 2.4 Measurement system

In this experiment, the acceleration signals measured from the accelerometers were amplified by the B&K NEXUS 2692 charge amplifier. The displacement signals from the laser displacement meters were conditioned by the LK 2503 conditioners (see Fig. 3(d)). Then all the conditioned displacement and acceleration responses together with the force signals were collected and processed by a 32-channel data acquisition system KYOWA EDX-100A, as shown in Fig. 3(c) and Fig. 5(b). The sampling rate was set as 1000 Hz. The flowchart of the measurement system is shown in Fig. 5(c).

## 3 Modelling and Model Updating

Before performing the proposed optimal sensor placement and response reconstruction algorithm, a concise finite element (FE) model should be built for the physical cantilever beam. Modal tests are then conducted to determine the dynamic properties of the cantilever beam and the model updating of the FE model was conducted using the measured modal properties so as to obtain an updated FE model that best represents the cantilever beam to be tested.

### 3.1 FE modelling

A FE model corresponding with the test beam was established in ANSYS 14.0 using the 2D Euler-Bernoulli beam elements. The FE model consisted of 16 equal length elements of 100 mm, 16 nodes (except for the fixed end), and a total of 48 DOFs (see Fig. 6(a)). The calculated first five natural frequencies are listed in Table 1. The calculated first three normalized displacement mode shapes and rotational mode shapes are shown in Figs. 6(b) and 6(c), respectively.

### 3.2 Modal test

Modal test was carried out to provide modal properties for updating the FE model and to check the functionality of the already installed sensors. Three laser meters and four accelerometers were employed to measure the structural responses. Before installing the exciter, the hammer impact was applied to the cantilever beam, and

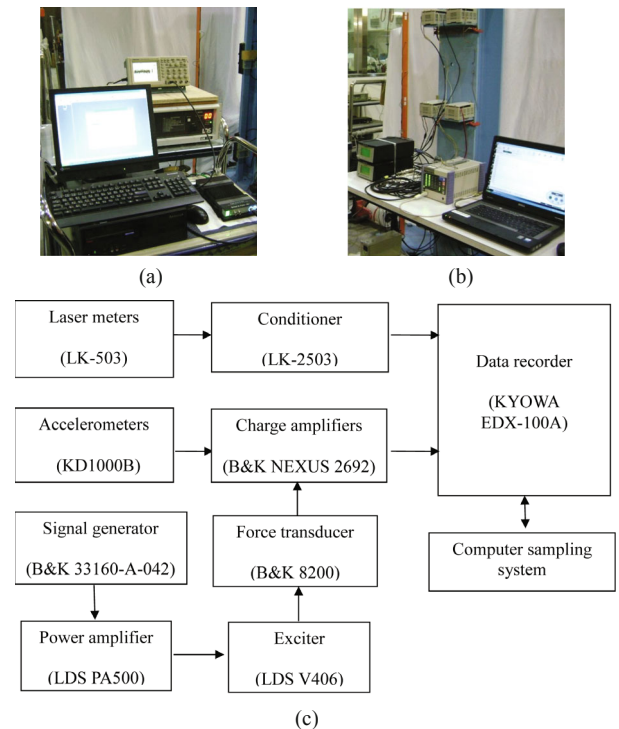
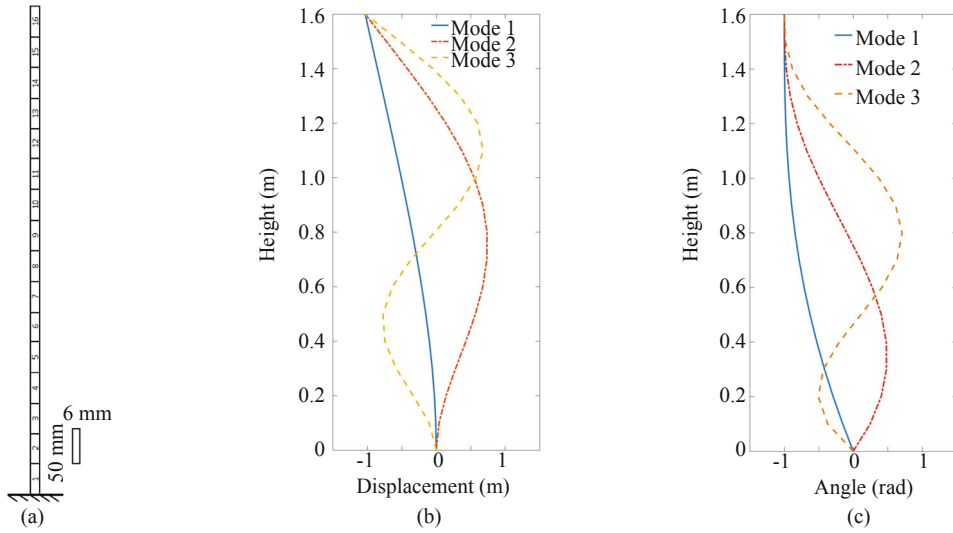
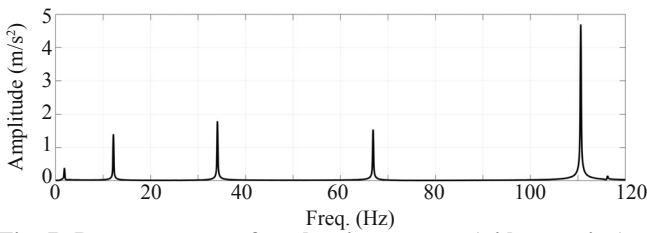


Fig. 5 Measurement setup: (a) excitation system; (b) sensor and data acquisition system; (c) flowchart



**Fig. 6** FE model and modal shapes of the cantilever beam: (a) FE model; (b) normalized displacement mode shapes; (c) normalized rotational mode shapes

the power spectra were then obtained through spectral analysis of the recorded structural responses. Figure 7 shows the power spectrum of one acceleration response, from which the natural frequencies of the beam could be identified and the results are listed in Table 1. After installing the exciter to the beam at 100 mm above the ground, a zero-mean random force with a bandwidth of 1.5-120 Hz was generated, and the structural responses were recorded. Figures 8(a) and 8(b) show the transfer function of displacement response measured by the laser meter and the transfer function of acceleration response measured by the accelerometer, respectively, from which the natural frequencies of the beam after installing the exciter could be identified and compared with those



**Fig. 7** Power spectrum of acceleration response (without exciter)

measured without the exciter (see Table 1). It can be seen from Table.1 that the first five natural frequencies are almost the same with a maximum error of 0.788% only and that the installation of the exciter has negligible influence on the dynamic properties of the beam. Table 1 also compares the measured and computed natural frequencies. It can be seen that the computed first natural frequency is 1.940 Hz while the measured one (with exciter) is 1.871 Hz. The relative error is 3.6%, indicating the necessity of model updating.

In addition to the modal frequencies, the modal shapes of the beam were also identified at the measurement points. The measured acceleration responses were first converted to the displacement responses through double integration and filtering, and they were then used together with the displacement responses measured by the laser meters to find the mode shapes. The comparison of the normalized first three mode shapes between the analyzed and measured results are shown in Fig. 9, and the comparative results are very satisfactory. The measured damping ratios of the first five modes of vibration of the beam were 0.17, 0.16, 0.12, 0.09 and 0.08%, which will be used in section 4 for response reconstruction.

**Table 1** Measured and computed natural frequencies of the beam

| Mode No. | Computed Frequency (Hz) | Measured Frequency (Hz)   |                          |                    |
|----------|-------------------------|---------------------------|--------------------------|--------------------|
|          |                         | Before installing exciter | After installing exciter | Relative Error (%) |
| 1        | 1.9395                  | 1.875                     | 1.871                    | -0.213             |
| 2        | 12.154                  | 12.188                    | 12.138                   | -0.41              |
| 3        | 34.033                  | 34.09                     | 33.892                   | -0.581             |
| 4        | 66.696                  | 66.88                     | 66.36                    | -0.778             |
| 5        | 110.28                  | 110.61                    | 110.11                   | -0.452             |

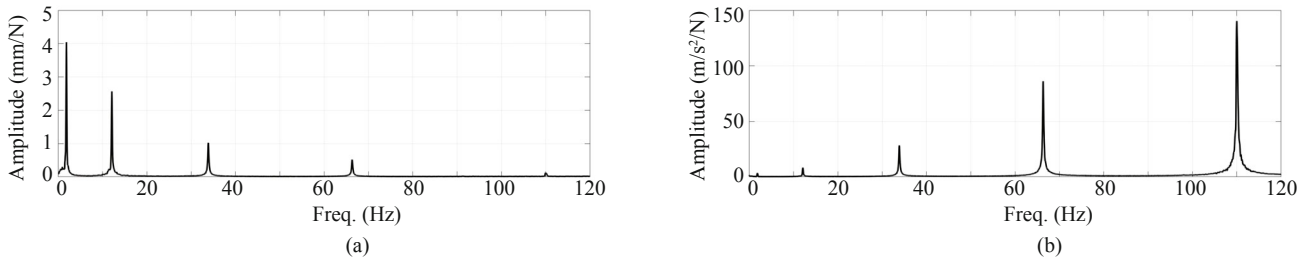


Fig. 8 Transfer functions: (a) displacement response; (b) acceleration response (with exciter)

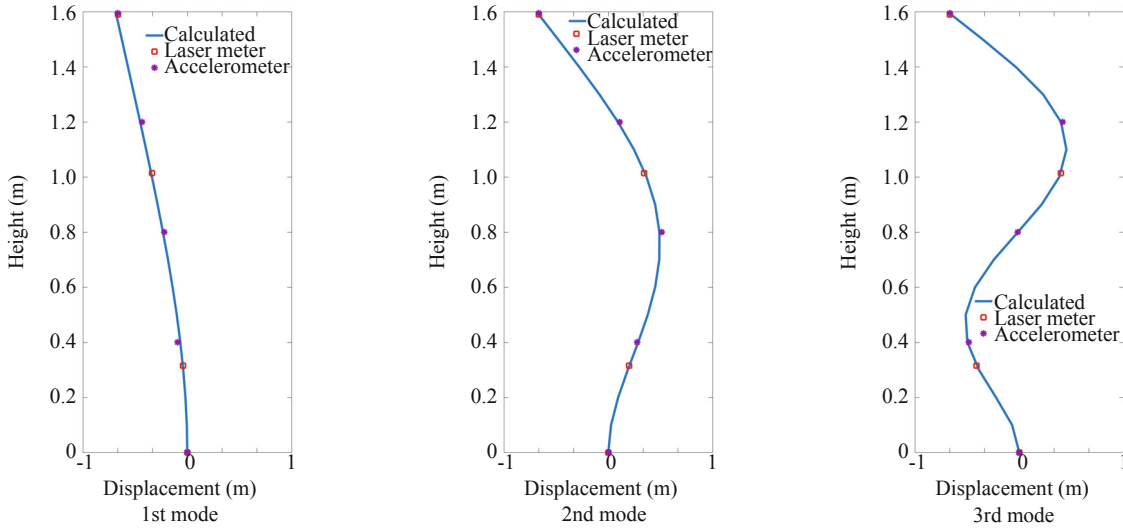


Fig. 9 Comparison of the measured and computed first three modal shapes of the beam

### 3.3 FE model updating

The model updating was conducted using the measured dynamic characteristics to ensure that the FE model of the beam could best represent the physical beam. The measured incomplete mode shapes were checked by the modal assurance criteria (MAC) which is defined as follows (Allemang and Brown, 1982):

$$\text{MAC}(\Phi_{ai}, \Phi_{ej}) = \frac{|\Phi_{ai}^T \Phi_{ej}|^2}{\|\Phi_{ai}^T \Phi_{ai}\| \|\Phi_{ej}^T \Phi_{ej}\|} \quad (3)$$

where  $\Phi_{ai}$  is the  $i$ th computed mode shape; and  $\Phi_{ej}$  is the  $j$ th measured mode shape. MAC matrix values vary between 0 and 1, and a MAC value close to 1 indicates a good correlation, whereas value close to 0 indicates a poor correlation

To minimize the differences in the first five frequencies and modal shapes between the computed and measured results, the objective function for model updating could be expressed as:

$$\text{ObjFun} = \sum_{i=1}^n a \left( \frac{f_i^a - f_i^m}{f_i^m} \right)^2 + \sum_{i=1}^n b \left( \frac{1 - \sqrt{\text{MAC}_i}}{\text{MAC}_i} \right)^2 \quad (4)$$

where  $f_i^a$  and  $f_i^m$  represent the computed and measured frequency of the  $i$ th mode;  $a$  and  $b$  are the weighing factors depending on the accuracy of identified natural frequencies and mode shapes. Because the measured modal frequencies have higher accuracy over the modal shapes, the values of  $a$  and  $b$  are taken as 1.0 and 0.1, respectively, in this study.

The four parameters were considered for model updating in consideration of their uncertainties and high sensitivities to the stiffness changes: Young's modulus, density, and thickness of the cantilever beam as well as the additional mass caused by the exciter and the force transducer. The optimization technique with a pattern search algorithm (Torczon, 1997) coded in MATLAB was adopted for the model updating. The first five natural frequencies and MAC values before and after model updating are listed in Table 2 and Table 3, respectively. It can be seen that after updating, all the errors between the computed and measured natural frequencies of the first five modes are less than 1%, and all the MAC values of the first five mode shapes are close to 1.0. Table 4 lists the changes in the updated parameters. These results indicate that the updated FE model can accurately represent the physical steel beam. The updated FE model described above was utilized for optimal sensor placement and response reconstruction in the subsequent study.

**Table 2 First five natural frequencies before and after model updating**

| Modes | Measured (Hz) | Before Updating |           | After Updating |           |
|-------|---------------|-----------------|-----------|----------------|-----------|
|       |               | Analyzed (Hz)   | Error (%) | Analyzed (Hz)  | Error (%) |
| 1     | 1.871         | 1.9395          | 3.6611    | 1.883          | 0.6414    |
| 2     | 12.138        | 12.154          | 0.1318    | 12.128         | -0.0824   |
| 3     | 33.892        | 34.033          | 0.4160    | 33.95          | 0.1711    |
| 4     | 66.36         | 66.696          | 0.5063    | 66.41          | 0.0753    |
| 5     | 110.11        | 110.28          | 0.1544    | 110.05         | -0.0545   |

**Table 3 First five MAC values before and after model updating**

| Modes | Before updating | After updating |
|-------|-----------------|----------------|
| 1     | 0.973           | 0.995          |
| 2     | 0.996           | 0.999          |
| 3     | 0.992           | 0.990          |
| 4     | 0.987           | 0.992          |
| 5     | 0.991           | 0.998          |

**Table 4 Updated parameters**

| Parameters for updating        | Initial values        | Updated values        | Change (%) |
|--------------------------------|-----------------------|-----------------------|------------|
| Young's Modulus (Pa)           | $2.06 \times 10^{11}$ | $2.08 \times 10^{11}$ | 0.97       |
| Density (kg/m <sup>3</sup> )   | 7800                  | 7895                  | 1.15       |
| Thickness (mm)                 | 6                     | 6.08                  | 1.33       |
| Additional mass of exciter (g) | 21                    | 18.9                  | -10        |

## 4 Multi-type sensor placement and response reconstruction

In this section, the integrated multi-type sensor placement and response reconstruction method is briefly introduced. This method is then applied to the updated FE model of the cantilever beam to find the optimal multi-type sensor placement. The accelerometers and laser displacement meters are then installed for the physical beam according to the calculated optimal sensor placement. A series of experiments were carried out, and the experimental results are finally used to validate the proposed method.

### 4.1 Basic theory

The equation of motion of a linear and elastic MOFs system under excitation  $\mathbf{u}$  can be expressed in the state-space:

$$\begin{cases} \dot{\mathbf{z}} = \mathbf{A}_c \mathbf{z} + \mathbf{B}_c \mathbf{u} \\ \mathbf{y} = \mathbf{C} \mathbf{z} + \mathbf{D} \mathbf{u} \end{cases} \quad (5)$$

where  $\mathbf{z}$  is the state vector;  $\mathbf{A}_c$  and  $\mathbf{B}_c$  are the state matrix and input matrix, respectively;  $\mathbf{C}$  and  $\mathbf{D}$  represent the output matrix and direct transmission matrix, respectively;  $\mathbf{y}$  is

the observation vector; and the state vector, state matrix and input matrix can be further expressed as

$$\mathbf{z} = \begin{Bmatrix} \mathbf{q} \\ \dot{\mathbf{q}} \end{Bmatrix}; \mathbf{A}_c = \begin{bmatrix} \mathbf{0} & \mathbf{I} \\ -\boldsymbol{\omega}_0^2 & -2\boldsymbol{\xi}\boldsymbol{\omega}_0 \end{bmatrix}; \mathbf{B}_c = \begin{bmatrix} \mathbf{0} \\ \boldsymbol{\Phi}^T \mathbf{L} \end{bmatrix} \quad (6)$$

where  $\mathbf{q}$  is the modal coordinate vector;  $\boldsymbol{\Phi}$  denotes the mass normalized translational displacement mode shapes;  $\boldsymbol{\xi}$  is the modal damping ratio matrix;  $\boldsymbol{\omega}_0$  is the modal frequency matrix;  $\mathbf{I}$  denotes the identity matrix; and the vector  $\mathbf{L}$  is used to designate the location of excitation.

In this study, the dynamic responses of a building structure, including the displacements, inclinations and accelerations at different levels, are merged in the observation vector  $\mathbf{y}$ .

$$\mathbf{y} = [\mathbf{d} \quad \boldsymbol{\theta} \quad \mathbf{a}]^T = \begin{Bmatrix} \boldsymbol{\Phi} \mathbf{q} \\ \boldsymbol{\Psi} \mathbf{q} \\ \boldsymbol{\Phi} \ddot{\mathbf{q}} \end{Bmatrix} \quad (7)$$

where  $\boldsymbol{\Psi}$  represents the rotational displacement modal shapes;  $\mathbf{d}$ ,  $\boldsymbol{\theta}$  and  $\mathbf{a}$  denote displacement, inclination and acceleration responses, respectively.

$$C = \begin{bmatrix} \Phi & 0 \\ \Psi & 0 \\ -\Phi\omega_0^2 & -2\Phi\xi\omega_0 \end{bmatrix}; D = \begin{bmatrix} 0 \\ 0 \\ \Phi\Phi^T L \end{bmatrix} \quad (8)$$

The continuous state space equation is then discretized in consideration of response measurements, and measurement noise  $w_k$  and process noise  $v_k$  are incorporated for real applications.

$$\begin{cases} z_{k+1} = Az_k + Bu_k + w_k \\ y_k^m = C^m z_k + D^m u_k + v_k \end{cases} \quad (9)$$

where  $z_k = z(k\Delta t)$  denotes the discrete time state vector;  $A = e^{A_c \Delta t}$  and  $B = \int_0^{\Delta t} e^{A_c \tau} d\tau B_c = A_c^{-1} (e^{A_c \Delta t} - I) B_c$ ;  $y_k^m$  refers to the sensor measurements;  $C^m$  and  $D^m$  consist of the mode shapes at the DOFs with sensors;  $w_k$  is the process noise caused by modeling inaccuracies; and  $v_k$  represents the measurement noise of sensors. Both noises are generally regarded as zero-mean white noise with variance matrices being  $Q = E(w w^T)$  and  $R = E(v v^T)$ , respectively, which are assumed as constants in this study.

Kalman filter is a well-recognized recursive algorithm that provides unbiased and optimal state estimation for a linear dynamic system from noise-contaminated measurement. Kalman filter algorithm is performed in the following two steps:

Time update:

$$\hat{z}_k^- = A\hat{z}_{k-1}^+ + Bu_{k-1} \quad (10)$$

$$P_k^- = AP_{k-1}^+ A^T + Q \quad (11)$$

Measurement update:

$$\hat{z}_k^+ = \hat{z}_k^- + K_k [y_k - C^m \hat{z}_k^- - D^m u_k] \quad (12)$$

$$P_k^+ = [I - K_k C] P_k^- \quad (13)$$

$$K_k = P_k^- C^{mT} [C^m P_k^- C^{mT} + R]^{-1} \quad (14)$$

where  $\hat{z}_k^-$  is defined as the priori state estimate at time step  $k$  given the process noise to step  $k-1$ , and  $\hat{z}_k^+$  denotes a posteriori state estimate at step  $k$  given the measurement  $y_k$ ; the subscript m refers to measurement;  $K_k$  is the optimal Kalman gain;  $P_k^-$  and  $P_k^+$  are the priori and posteriori state estimation error covariance, respectively. The flowchart of the two-step Kalman filter is illustrated in Fig. 10.

After the minimum-variance unbiased estimates  $\hat{z}_k^+$  is obtained by an iterative algorithm of the aforementioned two processes, the reconstructed responses  $y_k^e$  at the interested locations and their real values  $y_k^r$  are respectively obtained by

$$y_k^e = C^e \hat{z}_k^+ + D^e u_k \quad (15)$$

$$y_k^r = C^e z_k + D^e u_k \quad (16)$$

where the subscript e and r stand for estimation and real respectively.

The covariance matrix of the estimation error can be expressed as

$$\Delta = \text{cov}(y_k^r - y_k^e) = C^e (z_k - \hat{z}_k^+) C^{eT} = C^e P_k^+ C^{eT} \quad (17)$$

where  $P_k^+$  denotes the covariance matrix of the estimation error in the state vector.

Since the measurement of displacement, rotational angle and acceleration are in significantly different orders of magnitude, the output influence matrix  $C^m$  tends to be highly ill-conditioned in this study. Thus, the standard deviation of the sensor noise is employed to normalize the modal shapes to avoid the possible inaccuracy induced by matrix ill-condition (Zhu *et al.*,

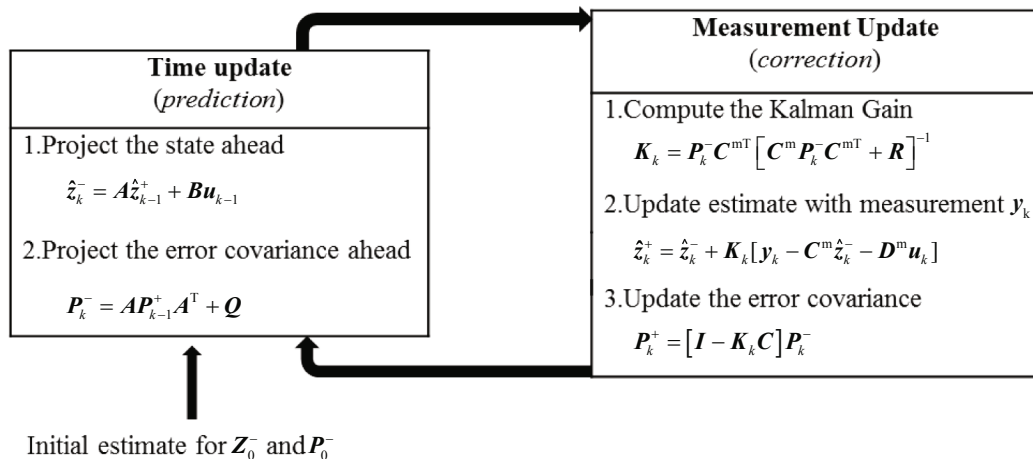


Fig. 10 Flowchart of the two-step Kalman filter

2013). The normalized  $\tilde{C}$  is given by

$$\tilde{C} = \begin{bmatrix} \Phi/\sigma_d & \mathbf{0} \\ \Psi/\sigma_\theta & \mathbf{0} \\ -\Phi\omega_0^2/\sigma_a & -2\Phi\xi\omega_0/\sigma_a \end{bmatrix} \quad (18)$$

where  $\sigma_d$ ,  $\sigma_\theta$  and  $\sigma_a$  represent the standard deviations of the noise from the laser meter, inclinometer and accelerometer, respectively.

The maximum and average estimation errors at all locations can be calculated by

$$\sigma_{\max}^2 = \max(\text{diag}(\tilde{\Lambda})) \quad (19)$$

$$\sigma_{\text{avg}}^2 = \frac{\text{tr}(\tilde{\Lambda})}{n} = \frac{\text{tr}(\tilde{C}^e P_k \tilde{C}^{eT})}{n} \quad (20)$$

The objective function and boundary condition can be defined as follows:

$$\text{ObjFun} = \min \left[ \text{trace}(\tilde{C}^e P_k \tilde{C}^{eT}) \right] \text{subject to } \tilde{\sigma}_{\max}^2 \leq \left[ \tilde{\sigma}_{\max}^2 \right] \quad (21)$$

where  $\left[ \tilde{\sigma}_{\max}^2 \right]$  represents the target maximum estimation error.

Through an iterative optimization procedure by deleting the candidate sensor locations during each iteration, the optimal locations and the minimal number of the three types of sensors can be determined to satisfy the preset minimum estimation error. In the meantime, the multi-scale responses at the key locations can be reconstructed using Eq. (15).

## 4.2 Optimal sensor placement

For the 16-nodes FE model of the cantilever beam, all the nodal horizontal displacements and accelerations except for the fixed end, as well as the rotational angle of each element, are the target responses to be measured or reconstructed. Thus, a total of 48 sensor locations were selected as initial candidates, including 16 for rotational angle sensors, 16 for displacement measurement sensors, and 16 for accelerometers. A random force with frequency ranging from 1.5 Hz to 120 Hz is applied to node 1 to excite the structure. The time history and Fourier amplitude of the excitation force measured from the force transducer are shown in Fig. 11. The first five modes which are within the excitation frequency bandwidth are selected to determine the number and optimal locations of the multi-type sensors. By the afore described procedure, the total number of sensors was determined by deleting the candidate sensor locations one by one until a target normalized estimated error threshold is reached. For a building structure, GPS

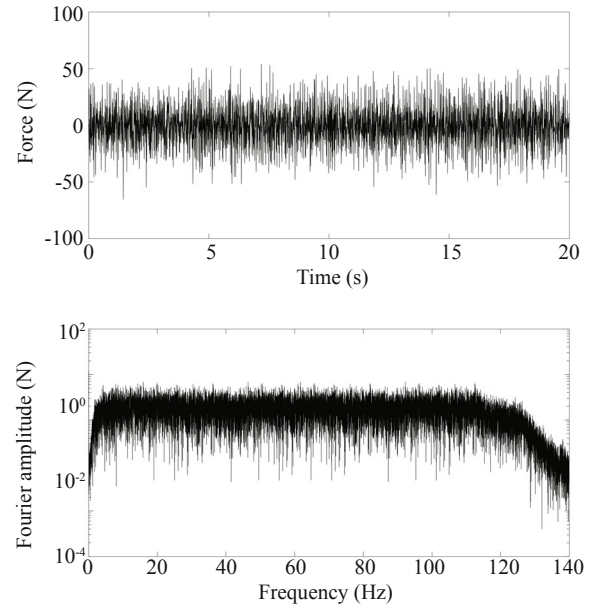


Fig. 11 Time history and Fourier amplitude of the input excitation (1.5-120 Hz)

receivers are sometime installed in the open area of the building, like on the platform or the roof, to measure the absolute displacement of the building. In this experimental investigation, one laser meter is present as the representative of a GPS receiver to measure the horizontal displacement of the beam and its location needs to be optimized by the proposed method. The maximum and average reconstruction error covariance increases with the deletion of candidate sensor number. When the deleted number of sensors increases to above 40 (48 in total), the maximum error exceeds the preset threshold of 1.0 and the reconstruction error increases sharply. Therefore, a total of eight sensor locations were selected, including three inclinometers, one laser displacement meter and four accelerometers (referred as OSP in the following sections), as listed in Table 5 and depicted in Fig.13. The optimized location to place one laser meter as a GPS receiver is on the top of the beam (Node. 16), indicating that the top floor displacement measurement is more informative than any other locations.

In the experiment, it is difficult to install the accelerometer and laser displacement meter at the exact location of node 16. Only a very close point was selected for measurement as substitution as shown in Fig.14. The actual responses of node 16 are then obtained by spline interpolation from the adjacent measurement point. The locations and installation of multi-type sensors are shown in Fig.14 and the exact locations of the multi-type sensors and force transducer are listed in Table 6.

## 4.3 Experiment results and validation

After installing the multi-type sensors according to their optimal locations determined by the proposed method, a series of experiments were carried out. This

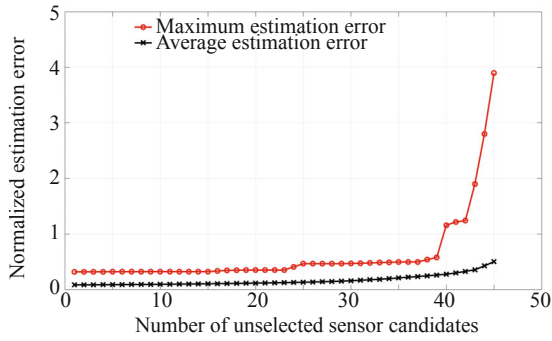


**Fig. 12 Variations of reconstruction errors with number of sensors**

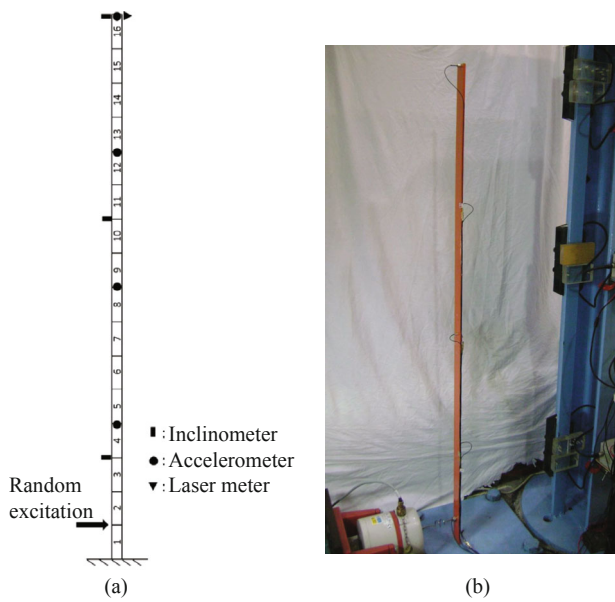


**Fig. 13 Optimal sensor placement configuration: (a) illustration; (b) lab view**

section presents the experimental results of the cantilever beam to evaluate the feasibility and effectiveness of the proposed method. The measurement data from the optimal multi-type sensor network were collected and then fused to estimate the key structural responses at the observed and unobserved locations. The reconstructed

displacement, acceleration and inclination responses of nodes 3, 10 and 16 were examined against the actual responses directly measured by the sensors (see Figs. 15-17). The actual acceleration responses of node 3 and node 10 are obtained from the corresponding measured displacement responses recorded by the laser meters through double differentials. The estimation errors are evaluated in terms of the relative percentage error (RPE) that is calculated using the following equation, where “std” represents the standard deviation,  $y^e$  and  $y^m$  are the estimated and measured time histories respectively.

$$RPE = \frac{\text{std}(y^e - y^m)}{\text{std}(y^m)} \times 100\% \quad (22)$$

Time-series comparison results depicted in Figs. 15, 16 and 17 show that the reconstructed responses almost overlap the measured responses for all three different kinds of responses at all three selected locations (nodes 3, 10, 16). The calculated RPEs as shown in Table 7 are all below 8%, which manifests a good match between the reconstructed and measured responses. It can also

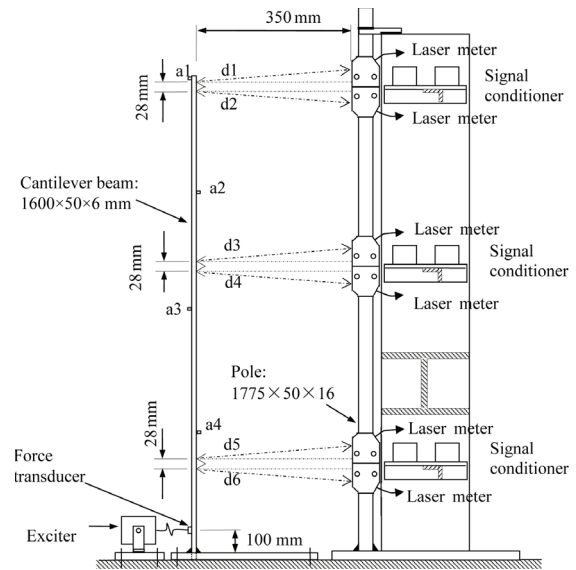


**Fig. 14 Locations and installation of multi-type sensors**

**Table 5 Optimal sensor placement solution**

| Sensor placement | Sensor type   | Sensor locations | Sensor number | Total |
|------------------|---------------|------------------|---------------|-------|
| OSP              | Inclinometer  | [3;10;16]        | 3             | 8     |
|                  | Accelerometer | [4;8;12;16]      | 4             |       |
|                  | Laser meter   | [16]             | 1             |       |

**Table 6 Exact locations of multi-type sensor and force transducer**

| Sensor      | Laser displacement meters |      |      |     |     |     | Accelerometers |      |     |     | Exciter |
|-------------|---------------------------|------|------|-----|-----|-----|----------------|------|-----|-----|---------|
|             | d1                        | d2   | d3   | d4  | d5  | d6  | a1             | a2   | a3  | a4  |         |
| Height (mm) | 1590                      | 1562 | 1014 | 986 | 414 | 386 | 1595           | 1200 | 800 | 400 | 100     |
| Node No.    | 16                        |      | 10   |     | 4   |     | 16             | 12   | 8   | 4   | 1       |

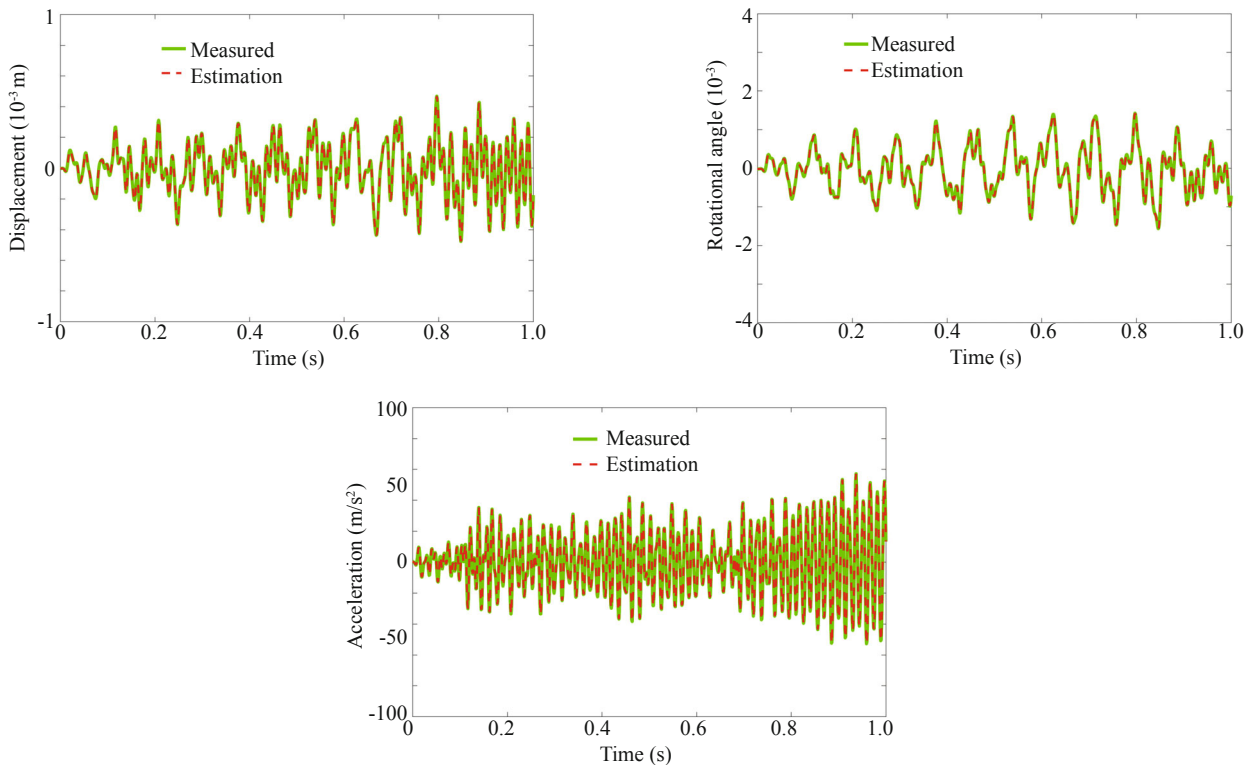


Fig. 15 Comparison of measured and estimated responses at node 3 (OSP)

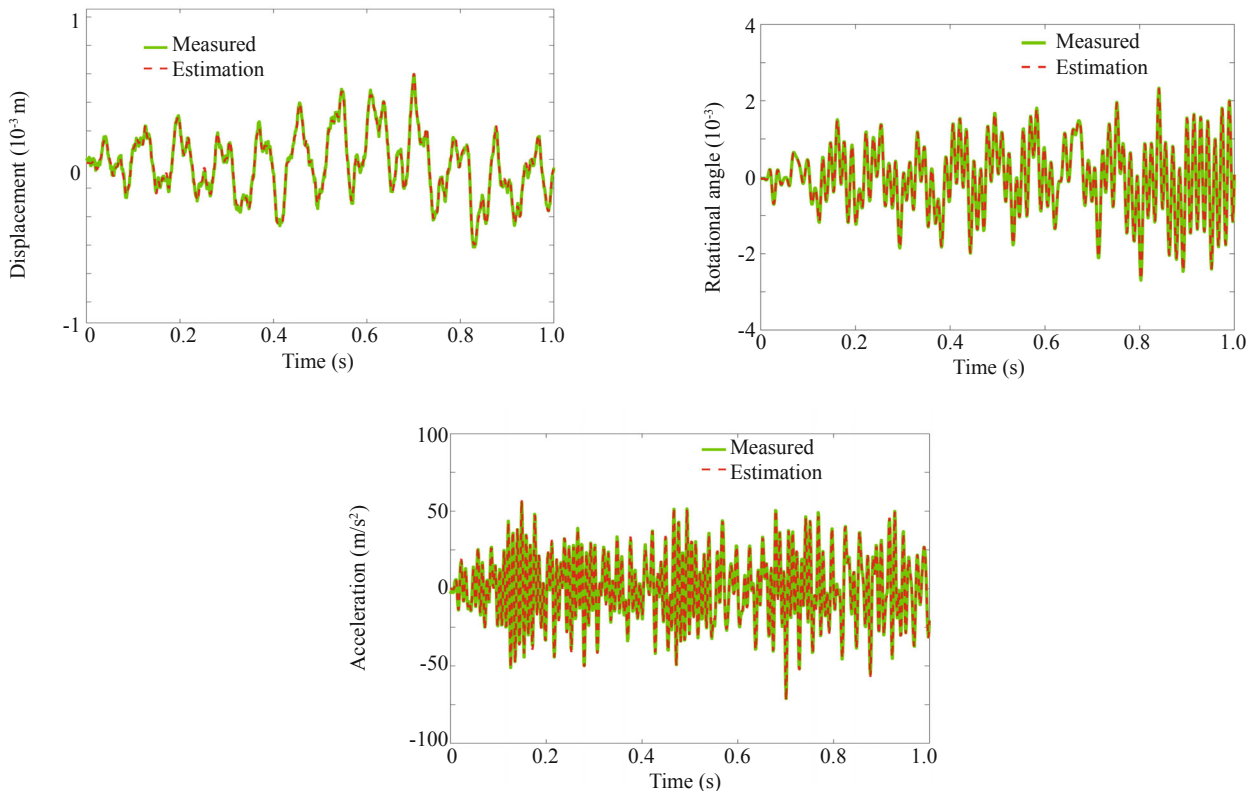


Fig. 16 Comparison of measured and estimated responses at node 10 (OSP)

be seen from Table 7 that the RPEs for the directly measured responses, which are also incorporated in the measurement function in the response reconstruction algorithm, are comparatively smaller than those

unobserved responses. It is clear that the measurement information could help improve the estimation accuracy. Thus, it is safe to draw a conclusion that the proposed response reconstruction method based on measurement

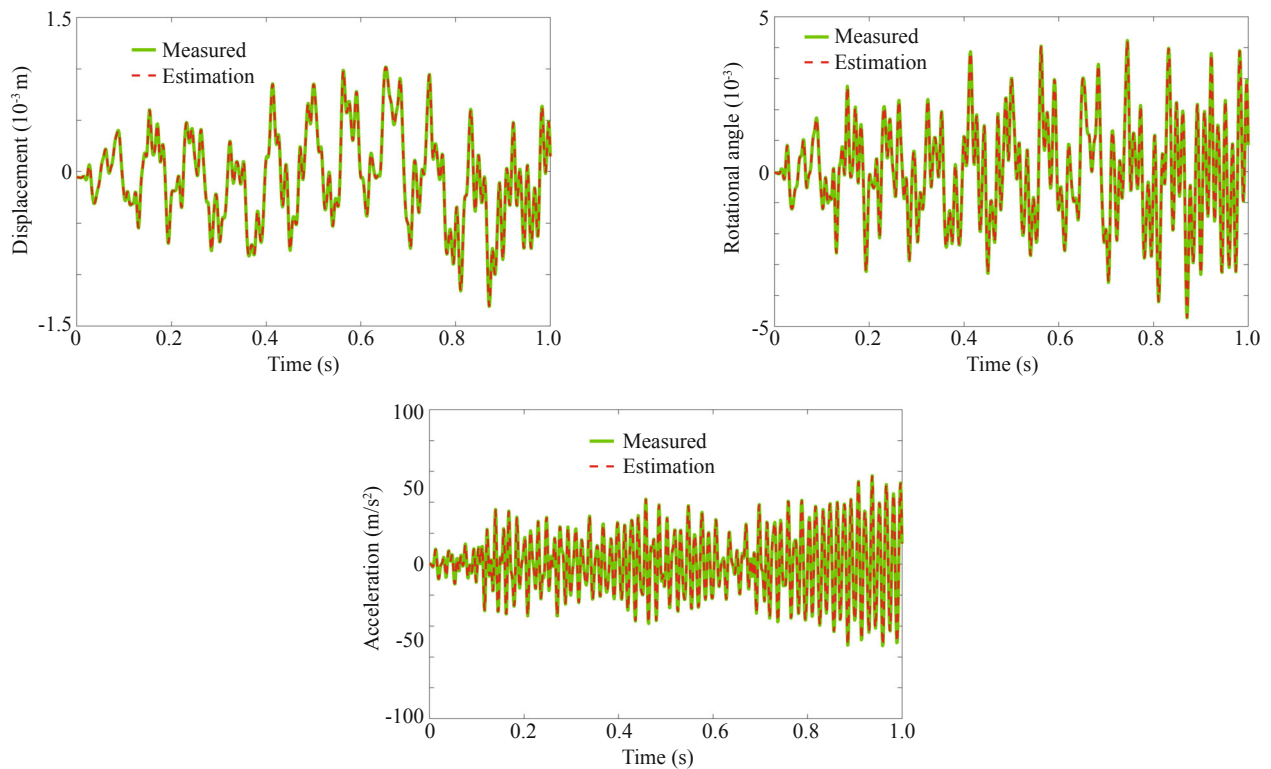


Fig. 17 Comparison of measured and estimated responses at node 16 (OSP)

Table 7 RPEs (%) of displacement, rotational angle and acceleration responses

| Node No. | RPEs (%)     |                  |              |
|----------|--------------|------------------|--------------|
|          | Displacement | Rotational angle | Acceleration |
| Node 3   | 6.32         | 3.59*            | 6.87         |
| Node 10  | 5.02         | 4.11*            | 7.33         |
| Node 16  | 4.38*        | 3.71*            | 3.56*        |

\*directly measured responses

data from optimized sensor locations could provide the unbiased estimation of structural state and response at all interested locations with and without sensor placement.

## 5 Further discussions

Additional experimental investigations were also conducted to check the robustness and applicability of the proposed method. Random excitations with three different bandwidths were applied separately to excite the physical beam to investigate the effect of excitation frequency range on the response reconstruction. Response reconstruction under unknown excitation was performed to manifest the potential of the method for estimating both response and excitation simultaneously. Two additional sensor placement strategies, namely the accelerometers-only placement and non-optimal sensor placement strategies, were also investigated and the results were compared with the optimal sensor placement scheme to demonstrate the impact of sensor types and sensor locations on the accuracy of response reconstruction.

### 5.1 Effect of excitation frequency range

Except for the 1.5–120 Hz random excitation applied in the experimental test, two other random excitations with quite different bandwidths: 1.5–35 Hz and 1.5–4.5 Hz, were also adopted to investigate the influence of excitation frequency ranges on the response reconstruction. The time history and Fourier amplitude of the excitation are shown in Figs.18 and 19, respectively, for case 2 and case 3.

Case 1: Random excitations with bandwidth: 1.5–120 Hz (to excite first five modes)

Case 2: Random excitations with bandwidth: 1.5–35 Hz (to excite first three modes)

Case 3: Random excitations with bandwidth: 1.5–4.5 Hz (to excite only first mode)

It can be seen that the excitations for case 1, case 2 and case 3 are very different. The response reconstruction is then performed for each loading case, and the comparison results of the unobserved responses at node 10 are selected for illustration. The time history comparison in Figs. 20 and 21 shows a good match between the measured and estimated acceleration and

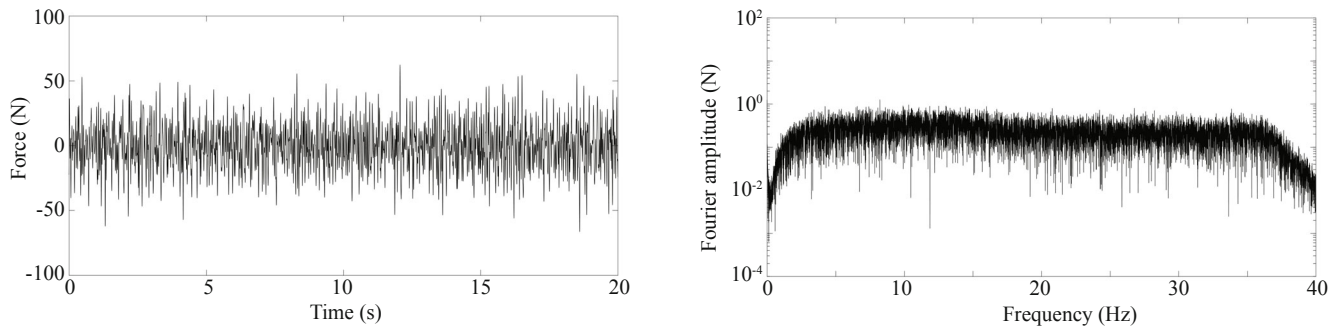


**Fig. 18** Time history and Fourier amplitude of the excitation (1.5-35 Hz) for case 2

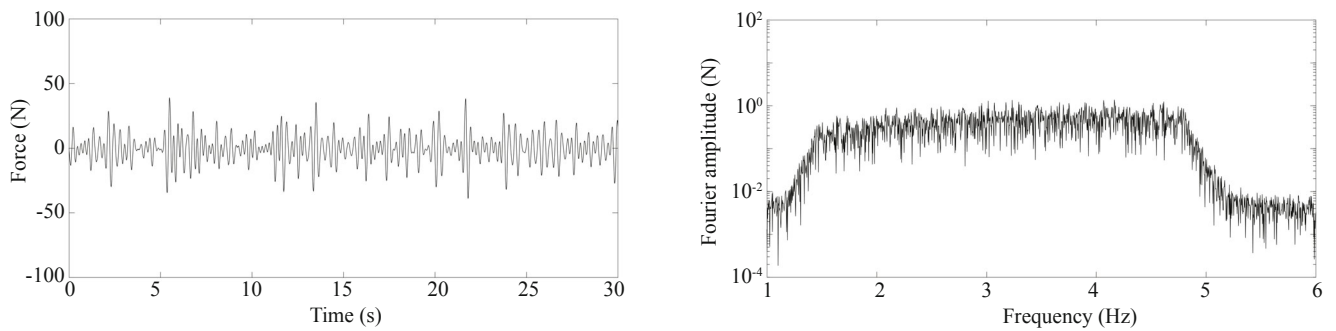


**Fig. 19** Time history and Fourier amplitude of the excitation (1.5-4.5 Hz) for case 3

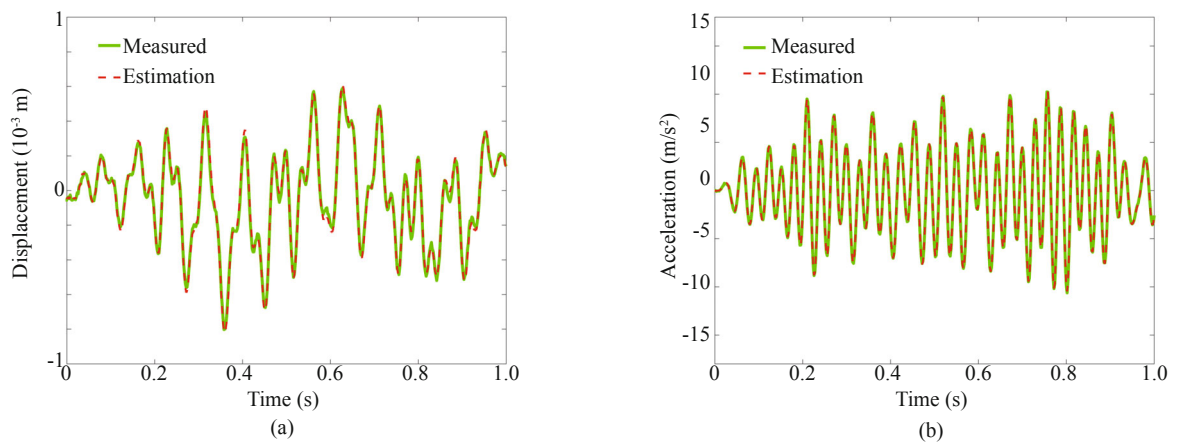


**Fig. 20** Comparison of measured and estimated responses at Node 10 (case 2)

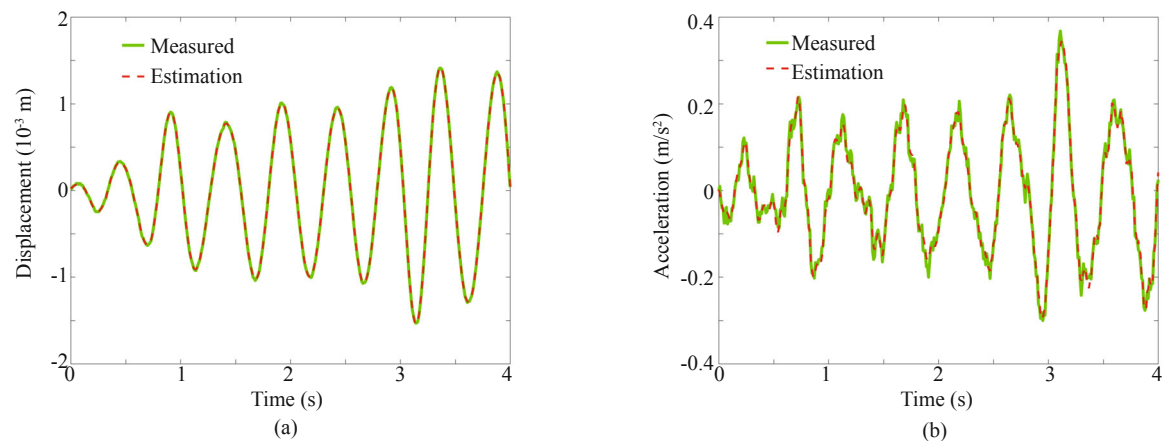


**Fig. 21** Comparison of measured and estimated responses at Node 10 (case 3)

**Table 8 RPEs (%) of displacement and acceleration responses for three different cases**

| Sensor placement | Response     | Node No. | RPEs (%) |        |        |
|------------------|--------------|----------|----------|--------|--------|
|                  |              |          | Case 1   | Case 2 | Case 3 |
| OSP              | Displacement | 10       | 5.02     | 3.12   | 2.34   |
|                  | Acceleration | 10       | 7.33     | 6.54   | 5.89   |

displacement responses at node 10 for case 2 and case 3, respectively. The calculated RPEs for all the three loading cases are within an acceptable range (<8%), and a decrease of RPE values from case 1 to case 3 could be noted from Table 8. Therefore, it can be seen that though the optimized sensor placement was determined by using random excitation with bandwidth being 1.5-120 Hz (case 1), the response reconstruction for case 2 (1.5-35 Hz) and case 3 (1.5-4.5 Hz) with reduced frequency bandwidths still achieved good response reconstruction results. Since less modes of vibration of the beam were excited in case 2 and 3, the optimal sensor placement determined in case 1, considering the first five modes, could provide redundancy of measurement information for the response reconstruction, which also explains the decreased RPEs from case 1 to case 3. It is reasonable to conclude that the optimal sensor placement method is robust for various loading conditions when the appropriate input excitation is employed in the sensor selection procedure.

## 5.2 Effect of unknown excitation

In practice, the excitation for a building structure could not be accurately measured. Thus, the response reconstruction under unknown excitation may be necessary. In such cases, the excitation turns from known input to a time history that needs to be estimated together with the structural state or structural responses. The basic theory for the integrated optimal sensor placement and response reconstruction method, presented in section 4.1, should be advanced (Zhang and Xu, 2016).

The minimum-variance unbiased estimate of the excitation  $\hat{\mathbf{u}}_k$  is obtained by Eq. (23) with the gain matrix

$$\hat{\mathbf{u}}_k = \mathbf{M}_k (\mathbf{y}_k^m - \mathbf{C}^m \hat{\mathbf{z}}_k^-) \quad (23)$$

$$\mathbf{M}_k = (\mathbf{D}^{mT} \tilde{\mathbf{R}}_k^{-1} \mathbf{D}^m)^{-1} \mathbf{D}^{mT} \tilde{\mathbf{R}}_k^{-1} \quad (24)$$

where

$$\tilde{\mathbf{R}}_k = \mathbf{C}^m \mathbf{P}_k^{z-} \mathbf{C}^{mT} + \mathbf{R} \quad (25)$$

The variance of the excitation estimation error is defined as

$$\mathbf{P}_k^u = E \left[ (\mathbf{u}_k - \hat{\mathbf{u}}_k) \cdot (\mathbf{u}_k - \hat{\mathbf{u}}_k)^T \right] = (\mathbf{D}^{mT} \tilde{\mathbf{R}}_k^{-1} \mathbf{D}^m)^{-1} \quad (26)$$

Then the error covariance matrix described as Eq. (11) in section 4.1 should be rewritten as:

$$\mathbf{P}_{k+1}^{z-} = [\mathbf{A} \ \mathbf{B}] \begin{bmatrix} \mathbf{P}_k^{z+} & \mathbf{P}_k^{zu} \\ \mathbf{P}_k^{uz} & \mathbf{P}_k^u \end{bmatrix} \begin{bmatrix} \mathbf{A}^T \\ \mathbf{B}^T \end{bmatrix} + \mathbf{Q} \quad (27)$$

$$\mathbf{P}_k^{zu} = (\mathbf{P}_k^{uz})^T = E \left[ (\mathbf{z}_k - \hat{\mathbf{z}}_k^+) \cdot (\mathbf{u}_k - \hat{\mathbf{u}}_k)^T \right] = -\mathbf{K}_k \mathbf{D}^m \mathbf{P}_k^u \quad (28)$$

where  $\mathbf{P}_k^{zu}$  denotes the cross covariance of estimation errors of both state and excitation. Consequently, the unbiased minimum-variance estimates of state and excitation are simultaneously derived using the recursive filter.

The accuracy of the response reconstruction can be evaluated by the estimation error between the reconstructed and real response, which is defined as follows:

$$\delta_k = \mathbf{y}_k^r - \mathbf{y}_k^e = (\mathbf{C}^e \mathbf{z}_k + \mathbf{D}^e \mathbf{u}_k) - (\mathbf{C}^e \hat{\mathbf{z}}_k^+ + \mathbf{D}^e \hat{\mathbf{u}}_k) = \mathbf{C}^e \tilde{\mathbf{z}}_k^+ + \mathbf{D}^e \tilde{\mathbf{u}}_k \quad (29)$$

The covariance matrix of the estimation error in Eq. (17) defined in section 4.1 should be rewritten as

$$\mathbf{A}_k = E \left[ \delta_k \delta_k^T \right] = [\mathbf{C}^e \ \mathbf{D}^e] \begin{bmatrix} \mathbf{P}_k^{z+} & \mathbf{P}_k^{zu} \\ \mathbf{P}_k^{uz} & \mathbf{P}_k^u \end{bmatrix} \begin{bmatrix} \mathbf{C}^{eT} \\ \mathbf{D}^{eT} \end{bmatrix} \quad (30)$$

By using the measured response data in section 4.4, the response reconstruction of the beam under unknown excitation is performed to estimate both the input force and the structural state simultaneously. Figure 22 shows the comparison between real and estimated excitation, and the calculated RPEs for node 10 are listed in Table 9. These results show a good potential for performing excitation estimation using the theoretical framework described in this section, and the proposed integrated optimal sensor placement and response reconstruction method turns out to be feasible and effective under both known and unknown excitation. Of course, the errors of the response reconstruction are relatively large for the case of unknown excitation.

## 5.3 Effect of sensor types and locations

To assess the superiority of the proposed optimal

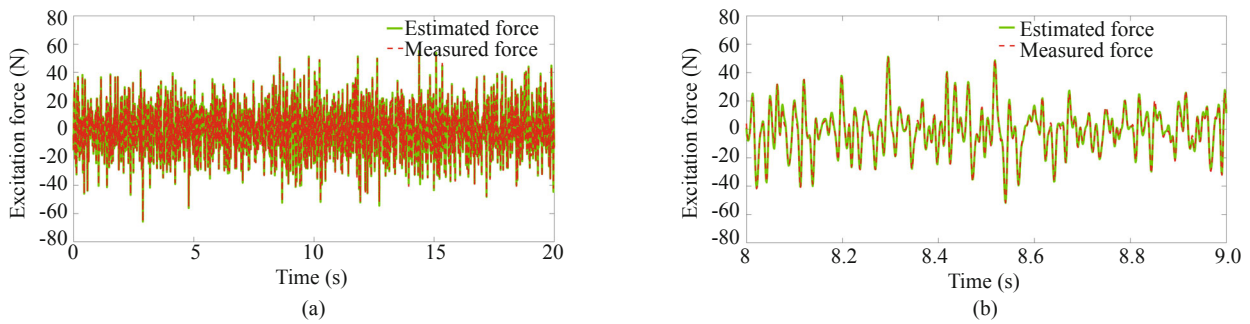


Fig. 22 Comparison of measured and estimated excitation: (a) the time history of excitation; (b) a close-up view of excitation time history

Table 9 RPEs (%) of displacement, rotational angle and acceleration responses as well as the input force under both known and unknown excitation

| Excitation | RPEs (%)     |                  |              |       |
|------------|--------------|------------------|--------------|-------|
|            | Displacement | Rotational Angle | Acceleration | Force |
| Known      | 5.02         | 4.11             | 7.33         |       |
| Unknown    | 7.62         | 5.58             | 8.74         | 16.3  |

placement method as well as to investigate the influence of sensor types and locations on the estimation error, two additional sensor placement schemes, namely SP1 and SP2, were also included for comparison with the optimal sensor placement scheme discussed in section 4.2, referred as OSP in this section. For the SP1 configuration, only eight accelerometers were arranged on the beam with equal space (at Node 2, 4, 6, 8, 10, 12, 14, 16). The SP2 sensor placement scheme adopted the same number of each type sensor with OSP, but the locations are chosen differently from OSP. The three sensor placement configurations are all shown in Fig. 23. The detailed arrangement is listed in Table 10.

Experiments were performed for SP1 and SP2 sensor placement scheme mainly by altering the sensor installation. The excitation used in SP1 and SP2 experiments was identical with that used in OSP experiment. The same response reconstruction procedure was employed and the comparison results between the estimated and measured responses were shown in Fig. 24 and Fig. 25. The calculated RPEs under three different sensor placement configurations are listed in Table 11. Only the comparison of the reconstructed responses were included to evaluate the effectiveness of the three different sensor placement schemes. In all three sensor placement schemes, the laser meters were installed at either node 9 (SP2) or node 10 (OSP, SP1) where the unobserved responses could be compared and the noise levels at the two adjacent nodes (100mm distance) were almost the same. Thus, responses at node 9 and node 10 were appropriate for comparison.

For the accelerometer-only sensor placement scheme (SP1), the RPEs between the measured and estimated displacement and rotational angle responses are over

10%, indicating a relatively poor estimation. The spikes observed from the time histories of the estimated displacement and rotational angle response could be attributed to the high frequency noises. Compared with the OSP and SP2 schemes adopting multi-type sensors, especially the inclinometers and the displacement meter on the top, it will be much unreliable to use only accelerometers to reconstruct lateral and rotational displacement responses for flexible building structure.

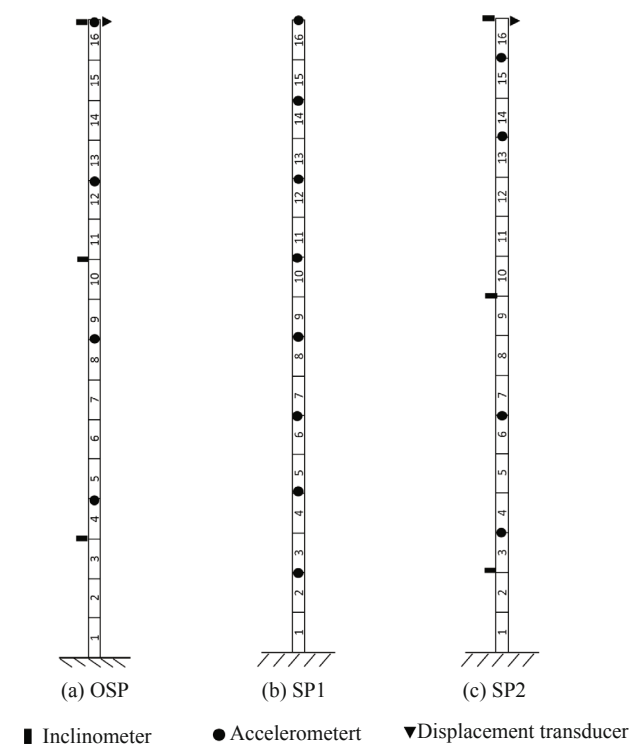
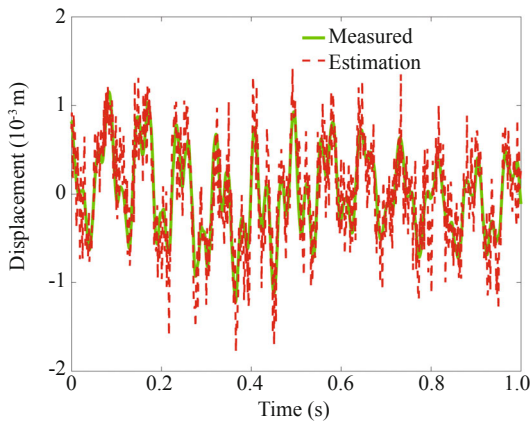


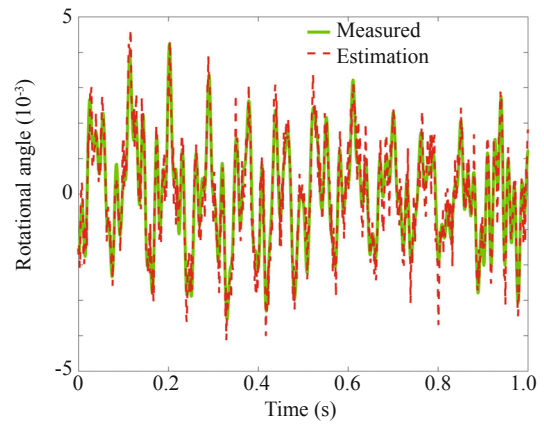
Fig. 23 Three different sensor placement configurations

**Table 10 Locations and numbers of three different sensor placement**

| Sensor placement | Sensor type   | Sensor locations      | Sensor number | Total number |
|------------------|---------------|-----------------------|---------------|--------------|
| OSP              | Inclinometer  | [3;10;16]             | 3             | 8            |
|                  | Accelerometer | [4;8;12;16]           | 4             |              |
|                  | Laser meter   | [16]                  | 1             |              |
| SP1              | Inclinometer  |                       | 0             | 8            |
|                  | Accelerometer | [2;4;6;8;10;12;14;16] | 8             |              |
|                  | Laser meter   |                       | 0             |              |
| SP2              | Inclinometer  | [2;9;16]              | 3             | 8            |
|                  | Accelerometer | [3;6;13;15]           | 4             |              |
|                  | Laser meter   | [16]                  | 1             |              |

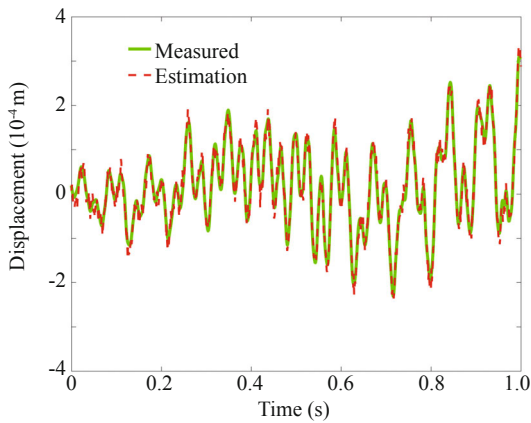


(a) Displacement of Node 10

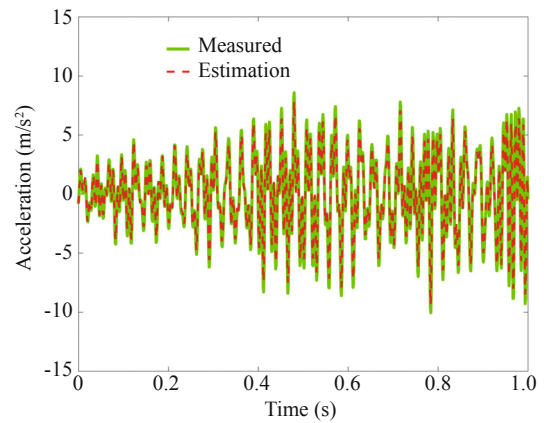


(b) Rotational angle of Node 10

**Fig. 24 Comparison of measured and estimated responses (SP1)**



(a) Displacement of Node 9



(b) Acceleration of Node 9

**Fig. 25 Comparison of measured and estimated responses (SP2)**

**Table 11 RPEs of the reconstructed and measured responses under three different sensor placement configurations**

| Sensor placement | Response         | Node No. | RPEs (%) |
|------------------|------------------|----------|----------|
| OSP              | Displacement     | 10       | 5.02     |
|                  | Acceleration     | 10       | 7.33     |
| SP1              | Displacement     | 10       | 16.32    |
|                  | Rotational Angle | 10       | 12.17    |
| SP2              | Displacement     | 9        | 6.22     |
|                  | Acceleration     | 9        | 10.21    |

For the non-optimal sensor placement (SP2) configuration, the RPEs of displacement and acceleration responses at node 9 were calculated for all the three loading cases. Since nodes 9 and 10 are close to each other, the noise levels are almost equal and the RPEs calculated for node 9 in SP2 situation are regarded comparable to those calculated for node 10 in OSP and SP1 situation. Compared with the optimal sensor placement strategy (OSP), the non-optimal placement (SP2) provides relatively poorer response estimation of the cantilever beam regarding to the nodal displacement and acceleration responses, which could be manifested by the larger RPEs in SP2.

It can be seen from the above discussion that although the sensor numbers for each type of sensor adopted in SP2 sensor placement scheme are the same with those adopted in OSP scheme, the calculated RPEs for the unobserved responses are larger. Thus, it can be concluded that the sensor placement does have a significant influence on the response reconstruction accuracy. On the other hand, the RPE of the displacement response is relatively smaller compared with the RPE of acceleration response. Noting that in both OSP and SP2 scheme the laser meter was installed for the displacement measurement of node 16, one may claim that the displacement measurement at the top of the building structure is informative and effective for the displacement response estimation. This conclusion also coincides with the phenomenon in section 4.4 that the optimized location for the only one laser meter is at node 16.

The comparison of the estimation results for all three different sensor placement schemes not only manifests the effectiveness and feasibility of the proposed optimal sensor placement and response reconstruction method for building structures with multi-type sensors but also reveal the superiority of the optimal sensor placement over other schemes, like the accelerometers-only scheme and non-optimal scheme.

## 6 Conclusions

The effectiveness of the proposed method has been demonstrated by virtue of the experimental investigation of a cantilever beam. The experimental results show that both excitation and response can be estimated simultaneously using the limited measurement data, and the dynamic responses at the locations where no sensors are installed can be reconstructed accurately. By comparing experimental results of different loading cases, the optimal sensor placement achieved by the proposed method shows its robustness and applicability in various loading conditions, provided that the external loading location, the mode number used in response reconstruction and environmental noise characteristics remain the same. Through comparison of the response reconstruction results of the cantilever beam between three different sensor placement schemes (OSP, SP1, SP2), the results reveal that the proposed optimal multi-

type sensor placement method has remarkable superiority compared with the alternative sensor placement configurations and a multi-type sensor system with inclinometers, accelerometers and displacement meters could provide more accurate and reliable monitoring for flexible building structures.

## Acknowledgement

The work described in this paper is financially supported by the Hong Kong Polytechnic University through the group project “Fundamentals of Earthquake Engineering for Hong Kong” (4-ZZCD) and the collaborative research project with Beijing University of Technology (4-ZZGD). The first author would like to thank the Hong Kong Research Grants Council (RGC) for providing him with the Hong Kong PhD Fellowship and the Faculty of Construction and Environment of The Hong Kong Polytechnic University for providing him with the one-year top-up studentship.

## References

- Allemang RJ and Brown DL (1982), “A Correlation Coefficient for Modal Vector Analysis,” *Proceedings of the 1st International Modal Analysis Conference*, **1**, SEM, Orlando, 110–116.
- Hu RP, Xu YL, Lu X, Zhang CD, Zhang QL and Ding JM (2017), “Integrated Multi-Type Sensor Placement and Response Reconstruction Method for High-Rise Buildings Under Unknown Seismic Loading,” *Journal of The Structural Design for Tall and Special Buildings*. (in print)
- Li X, Rizos C, Tamura Y, Ge L, Yoshida A and Cranenbroeck J (2010), “Fundamental Bending Mode and Vibration Monitoring with Inclinometer and Accelerometer on High-Rise Buildings Subject to Wind Loads,” *Proceeding of the 5th World Conference on Structural Control and Monitoring*, Tokyo, Japan, 1–15.
- Su JZ, Xia Y, Chen L, Zhao X, Zhang QL, Xu YL, Ding JM, Xiong HB, Ma RJ, Lv XL and Chen AR (2013), “Long-Term Structural Performance Monitoring System for the Shanghai Tower,” *Journal of Civil Structural Health Monitoring*, **3**(1): 49–61.
- Torczon V (1997), “On the Convergence of Pattern Search Algorithms,” *SIAM Journal on Optimization*, **7**(1): 1–25.
- Xu YL, Zhang XH, Zhu S and Zhan S (2016), “Multi-Type Sensor Placement and Response Reconstruction for Structural Health Monitoring of Long-Span Suspension Bridges,” *Science Bulletin*, **61**(4): 313–329.
- Yigit CO, Li X, Inal C, Ge L and Yetkin M (2010), “Preliminary Evaluation of Precise Inclination Sensor and GPS for Monitoring Full-Scale Dynamic Response of a Tall Reinforced Concrete Building,” *Journal of Applied Geodesy*, **4**(2): 103–113.
- Yi TH, Li HN and Gu M (2011), “Optimal Sensor

Placement for Health Monitoring of High-Rise Structure based on Genetic Algorithm,” *Mathematical Problems in Engineering*, 1–12.

Zhang CD and Xu YL (2016), “Optimal Multi-Type Sensor Placement for Response and Excitation Reconstruction,” *Journal of Sound and Vibration*, **360**:

112–28.

Zhu S, Zhang XH, Xu YL and Zhan S (2013), “Multi-Type Sensor Placement for Multi-Scale Response Reconstruction,” *Advances in Structural Engineering*, **16**(10): 1779–97.